Hindawi
International Journal of Antennas and Propagation
Volume 2020, Article ID 5835620, 15 pages
https://doi.org/10.1155/2020/5835620

Research Article

Ship Velocity Estimation in Airborne Along-Track Interferometric SAR Imagery Based on the Fractional Fourier Transform

Chao Chen,[1] Yan Li,[1] Kuihua Huang,[1] Yonghong Long,[2] Linlin Zhang,[3] and Kewei Ouyang[4]

[1]*College of System Engineering, National University of Defence Technology, Changsha 410073, China*
[2]*College of Traffic Engineering, Hunan University of Technology, Zhuzhou 412007, China*
[3]*Faculty of Geoscience and Environmental Engineering, Southwest Jiaotong University, Chengdu 611756, China*
[4]*College of Electronic Science, National University of Defence Technology, Changsha 410073, China*

Correspondence should be addressed to Linlin Zhang; zhanglinlin@my.swjtu.edu.cn

Received 19 May 2020; Revised 9 October 2020; Accepted 24 October 2020; Published 16 November 2020

Academic Editor: Chien-Jen Wang

Synthetic aperture radar (SAR) was originally exploited to image stationary scenes. However, it is important to derive target information of velocity for many applications. The fractional Fourier transform (FrFT) is a generalization of the classical Fourier transform and is well-known as a useful tool to estimate the chirp rate of linear frequency-modulated (LFM) signals. Motion compensation is critical to moving target imaging. It is difficult for us to obtain the actual motion parameters in real scenarios. Based on the moving target echo model in airborne along-track interferometric SAR (ATI-SAR) and expression of the ATI phase, a method is proposed to estimate the ship velocity by combining the ATI phase with FrFT. First, we use the FrFT to evaluate the chirp rate of the moving target echo. Then, we construct an equation to estimate the ship velocity using the chirp rate estimation, peak response time, and ATI phase. Finally, the simulation experiments are used to validate the effectiveness of the proposed method.

1. Introduction

Sea traffic monitoring is one of the most important applications of synthetic aperture radar (SAR) imagery. Moving ship detection is an important issue in sea traffic monitoring, and imagery quality has a great impact on detection performance. Unfortunately, conventional imaging algorithms, such as Range-Doppler (RD), Chirp Scaling (CS), and SPECAN [1], have focused on static scenes. The performances of these imaging algorithms for moving targets worsen due to the motion of the target. SAR signatures of moving targets suffer from azimuthal displacement, smearing, defocusing caused by motion in the range direction, and loss of focus due to azimuthal velocity [2]. One solution that can address this problem for moving target imaging is motion compensation. By combining motion compensation with conventional imaging algorithms, it is possible to focus on moving targets. Motion compensation relies on the acquiring of motion parameters, i.e., velocities, for a target. Generally, utilizing the Automatic Identification System (AIS) conveniently provides the motion parameters of a moving target. Unfortunately, in many cases, no AIS data are available for moving targets. Therefore, an alternative method to realize velocity estimations should be explored.

Research on velocity estimation was first applied using ground moving target indication (GMTI). The challenge for GMTI is separating the returned signal of the moving target from the stationary background [3]. However, compared with a target moving across the ground, the stationary hypothesis is invalid in the wide ocean area due to different phenomena, such as ocean waves or moving ships [4]. Accordingly, it is not an easy task to estimate velocity for moving ships in the ocean.

Estimation methods for ship velocity have been extensively investigated in recent years. Methods can be roughly divided into two categories. The first category is based on ship wakes. Ship wakes have an important function in ship

detection and can be used to measure ship velocity. In SAR images, a ship wake appears like a fan of bright line-shaped features around a central dark line [5]. Tunaley [6] exploited the cross-range separation between a ship's location and its wake to estimate ship speed in images. Zilman et al. [7] observed Kelvin and turbulent wakes, and analysed the spectrum peak of ship-generated waves along the Kelvin cusp-lines to estimate ship speed. Copeland et al. [8] applied localized Radon transform to detect ship wakes in SAR. Courmontagne [9] exploited the stochastic match filtering technique to improve the detection performance of Radon transform. Carona and Marques [10] presented a strategy using the Radon transform to detect ship wakes and then estimate the range velocity component. Nevertheless, ship wakes are not always visible in SAR images. For example, with specific reference to RADARSAT-2 imagery, ship wakes associated with detected ships have been detected in less than 5% of cases [11].

The second category is based on Doppler parameter estimation because Doppler parameters are directly related to the motion parameters of a moving target. Compared with methods based on ship wakes, the methods in the second category have wider applications to ship velocity estimation. Renga and Moccia [12] proposed a ship velocity method for SAR images. The method measures the Doppler centroid of a ship candidate when the main feature of the ship is clearly imaged and the relevant complex pixels can be isolated from the background. Radius and Marques [13] proposed estimating the velocity vector of a moving ship in single-look complex (SLC) SAR data from antenna pattern effects induced by target motion. Dragosevic and Vachon [14] described a novel method for the radial component of a ship's velocity using single-channel synthetic aperture radar acquired by RADARSAT-1, which is applicable in the absence of visible wakes. Kirscht [15] assessed the temporal correlation between sublook images, which can be used to track vessel motion. Time-frequency processing is a powerful tool for analysing the properties of a linear frequency-modulated (LFM) signal, and the fractional Fourier transform (FrFT) is the representative in the processing. Pelich et al. [16] estimated the azimuth velocity component in SAR images based on the FrFT. However, they neglected the effect of range velocity and range acceleration components. Huang et al. [17] utilized Radon-high-order time-chirp rate transforms to refocus on fast moving ground targets and estimate high-order motion parameters. The method concurrently addresses the range walk and Doppler frequency shift in the presence of Doppler ambiguity, which could be generalized to estimate ship velocity. However, in the case of low signal-to-clutter ratio (SCR), the estimation performance of low-order motion parameters degraded because of the error propagation effect. In addition to these two categories of methods, there are others. For example, Soccorsi and Lehner [18] applied change detection techniques to a time series to estimate ship speed, and Ao et al. [19] proposed a moving ship velocity estimation method based on subaperture decomposition. Filippo [20] applied pixel tracking and convex optimization to achieve micromotion and inclination angle estimation. Back et al. [21] used the Doppler parameter estimation to estimate two-dimensional vessel velocity.

To summarize, these methods are usually based on single-channel SAR. However, the performance of these algorithms is limited by the signal-to-clutter-plus-noise ratio (SCNR) [22]; it is difficult to separate the target from the clutter background. These methods can barely estimate multiple motion parameters simultaneously with high accuracy; often, they achieve only one parameter estimation, such as range velocity or azimuth velocity. With the advent of multichannel SAR systems, additional echo information can be obtained and clutter can be suppressed more; therefore, more attention has been attracted for moving target indication (MTI) in multichannel than in single-channel applications. Three techniques have dominated the literature over the last few decades, displaced phase centre antenna (DPCA) [22], along-track interferometry (ATI) [23], and space-time adaptive processing (STAP) [24]. This has led to a breakthrough in applications to ship detection and velocity estimation. For example, in [25], Dragosevic et al. combined adaptive beamforming and frequency tracking, with ATI to estimate ship speed. Jiang et al. [26] applied FrFT to processing and used DPCA ship signatures in the range-compressed domain to achieve their goals. Chiu [27] proposed a settlement based on FrFT and ATI in the range-compressed domain. Cerutti-Maori et al. generalized the DPCA and STAP processing from a dual-channel SAR system to any multichannel SAR system, termed extended DPCA (EDPCA) and imaging STAP (ISTAP) in [27, 28], respectively. These modified techniques can also be used to estimate ship speed.

The SAR moving target velocity estimation can be achieved using two means, for both single-channel and multichannel. The first class of algorithm is implemented on the raw data or range-compressed domain, and the second class is implemented on the focused SAR image. For estimating velocity in multichannel SAR, which is the objective in this study, the algorithm proposed in [27] for data or the range-compressed domain has excellent proven performance. However, operator-friendly image-type products are sometimes preferred [29]. This paper focuses on developing a ship velocity estimation algorithm for the image domain in the dual-channel ATI-SAR mode. The proposed algorithm works on processed images for dual-channel SAR systems rather than range-compressed domain, which could estimate multiple motion parameters simultaneously.

The remainder of this paper is organized as follows. In Section 2, we provide an overview on the moving target echo model and ATI phase. Section 3 introduces the definition and properties of FrFT and the proposed method that combines the ATI phase with FrFT to estimate the motion parameters of a moving ship. In Section 4, we compare our method with the method provided in [16] in the image domain. Finally, summaries and conclusions are provided in Section 5.

2. Overview on the Moving Target Echo Model and ATI Phase

ATI-SAR is a technique initially applied to measuring ocean currents [30] and has since been used to detect slow-moving objects, such as vehicles and ships [31], and estimate the velocity of moving targets and river [32–35]. Obtaining velocity estimates of moving targets is an important goal of SAR-based moving target indication (MTI). Estimated outputs are often a combination of range, bearing, and Doppler frequency. The moving target echo model has a huge impact on velocity estimation; that is, the model accuracy has a great influence on algorithm accuracy, and the ATI phase has a proven ability to estimate radial velocity [35]. Therefore, in this section, we provide a brief overview of the echo model for moving targets and expression of the ATI phase used in our proposed method.

2.1. Moving Target Echo Model. The target and radar geometry for airborne SAR is illustrated in Figure 1, modified from [36]. In this figure, x denotes the along-track direction, y represents the across track direction, the initial coordinate of platform is $(0, 0, H)$, and the target is located at $(0, y_0, 0)$ when $t = 0$, assuming the target moves with velocity components (v_{x0}, v_{y0}) and acceleration components (a_{x0}, a_{y0}). The symbol v_a indicates the platform velocity, and R_0 is the distance between the target and radar at $t = t_0$, i.e., the nearest distance.

According to the geometry shown in Figure 1, we can obtain the range equation between the target and radar as [36]

$$R(t) = \left(\left(v_{x0}t + \frac{a_{x0}}{2}t^2 + \frac{\dot{a}_{x0}}{6}t^3 - v_a t \right)^2 + \left(y_0 + v_{y0}t + \frac{a_{y0}}{2}t^2 + \frac{\dot{a}_{y0}}{6}t^3 \right)^2 + H^2 \right)^{(1/2)}. \tag{1}$$

In general, we apply the approximate expression of (1) using the Taylor series expression [37]; applying the second-order Taylor series expression, equation (1) can be rewritten as [36]

$$R(t) \approx R_0 + \frac{y_0 v_{y0}}{R_0}t + \frac{1}{2R_0} \cdot \left[(v_{x0} - v_a)^2 + v_{y0}^2 \left(1 - \frac{y_0^2}{R_0^2} \right) + y_0 a_{y0} \right] t^2. \tag{2}$$

The approximation shown in the above expression is based on the following fact, i.e., the influence of the third and higher order terms of the Taylor series expression is relatively small because the values of acceleration and the rate of change of acceleration are too small for the distance between the radar platform and the target. The distance between the phase centres of two antennas in a dual-channel system is d, and distance from the radar platform to the target is assumed to be large enough so that the far-field approximation can be applied [36].

The moving target echo model in terms of range history can be expressed as follows [36]:

$$\begin{aligned} s_i(t) = A_i(u_i(t)) \exp\left(-jkR_i^{\text{two-way}}(t) \right) \\ \cdot \operatorname{rect}\left(\frac{t}{T} \right), \quad i = 1, 2, \end{aligned} \tag{3}$$

where $A_i(u)$, $i = 1, 2$ is the magnitude of the fore channel and aft channel, respectively, $R_i^{\text{two-way}}(t)$, $i = 1, 2$ is the range from the transmitting antenna to the moving target and back to the two receive antennas, $k = 2\pi/\lambda$ is the wave number, and rect is a rectangle window centred at $t = 0$ of length T.The difference in the received echo between the fore and aft channel results from $R_i^{\text{two-way}}(t)$. For the fore channel, the range can be denoted by

$$R_1^{\text{two-way}}(t) = 2R(t). \tag{4}$$

On the basis of (4), the range of the aft channel can be expressed using a function of $R_1(t)$ as

$$R_2^{\text{two-way}}(t) = 2R(t) + \delta R(t). \tag{5}$$

Furthermore, the expression of $\delta R(t)$ was derived in [38] as

$$\delta R(t) = d \left(\frac{(v_{x0} - v_a)t + (1/2)a_{x0}t^2 + (1/6)\dot{a}_{x0}t^3}{R_1(t)} \right). \tag{6}$$

In [39], the first-order Taylor series expression was used to approximate (6), that is,

$$\delta R(t) = d \frac{(v_{x0} - v_a)}{R_0}t. \tag{7}$$

For the any given sample time t' for the fore channel, the range to the target at time $t' + (d/(2v_a))$ should be determined for the aft data to line up the channels. The registered aft channel can be expressed as

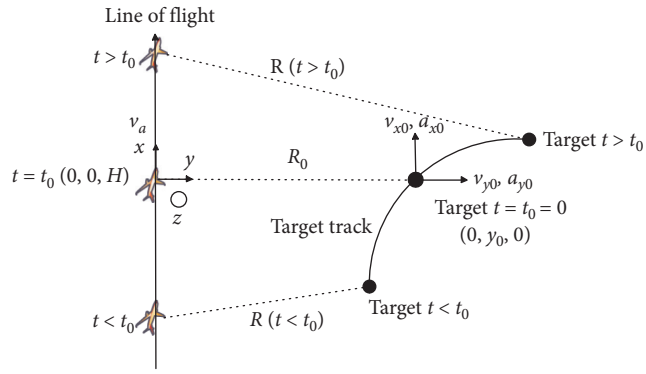

Figure 1: Target and radar geometry for the airborne case [36].

$$R_{2.\mathrm{reg}}^{\mathrm{two-way}}(t) = 2R\left(t + \frac{d}{2v_a}\right) + \delta R\left(t + \frac{d}{2v_a}\right). \tag{8}$$

Substituting (2) and (8) into (4) and (5), the following equations can be obtained:

$$R_1^{\mathrm{two-way}}(t) = 2\left\{R_0 + \frac{y_0 v_{y0}}{R_0}t + \frac{1}{2R_0}\cdot\left[(v_{x0} - v_a)^2 + v_{y0}^2\left(1 - \left(\frac{y_0^2}{R_{0.}^2}\right)\right) + y_0 a_{y0}\right]t^2\right\}, \tag{9}$$

$$\begin{aligned} R_{2.\mathrm{reg}}^{\mathrm{two-way}}(t) = {} & 2\left[R_0 + \frac{y_0 v_{y0}}{R_0}\left(t + \frac{d}{2v_a}\right)\right] + d\frac{(v_{x0} - v_a)}{R_0}\left(t + \frac{d}{2v_a}\right) \\ & + \frac{1}{R_0}\cdot\left[(v_{x0} - v_a)^2 + v_{y0}^2\left(1 - \frac{y_0^2}{R_{0.}^2}\right) + y_0 a_{y0}\right]\left(t + \frac{d}{2v_a}\right)^2. \end{aligned} \tag{10}$$

Substituting (9) and (10) into (3), we obtain detailed expressions of the moving target echo for the fore and aft channels; then, the established moving target echo model is used to calculate the ATI phase. The model characterized with formula (24) is an approximation of the real scenario. The more precise model should consist of motion in three directions, i.e., roll, yaw, and heave. Roll and yaw are considered in formula (24), but heave motion is neglected, for more complex models making it more difficult to retrieve parameters from the model. At present, it is not realistic to solve the task including six unknown parameters, i.e., velocity and acceleration in three directions. To the best of our knowledge, the model in [40, 41] has not been used in the published literature to estimate motion parameters in three directions simultaneously. Moreover, the velocity information for range and azimuth contained in the model shown in formula (24) might be sufficient for practical applications, such as ship location and refocusing.

2.2. ATI Phase. From these described derivations, we can obtain the ATI phase using conjugate multiplication. However, the ATI operator is often achieved in the azimuth-compressed domain [36]. The relationship between the original echo and azimuth-compressed echo is as follows:

$$I_i(t) = \frac{1}{T}\int_{-\infty}^{\infty} s_i(t + \tau) r_i^*(\tau)\mathrm{d}\tau, \tag{11}$$

where $I_i(t)$ is the compressed azimuth signal for the i channel and $r_i(t)$ is the reference function.

According to (11), we can derive the expression $I_i(t) = (1/T)\int_{-\infty}^{\infty} s_i(t + \tau) r_i^*(\tau)\mathrm{d}\tau$ or peak response time t_{img} for the fore channel ($i = 1$) and ATI phase $\angle$ATI as

$$t_{\text{img}} = \frac{-y_0 v_{y0}}{\left(v_{x0} - v_a\right)^2 + v_{y0}^2\left(1 - \left(y_0^2/R_0^2\right)\right) + y_0 a_{y0}}, \tag{12}$$

$$\angle\text{ATI} = \frac{k\, d\, y_0 v_{y0}}{2R_0} \cdot \left(\frac{1}{v_a} - \left(\frac{\left(v_{x0} - v_a\right)}{\left(v_{x0} - v_a\right)^2 + v_{y0}^2\left(1 - \left(y_0^2/R_0^2\right)\right) + y_0 a_{y0}}\right)\right). \tag{13}$$

The detailed derivation can be found in [36]. It should be noted that the fitting condition of the equation (12) is target's azimuth coordinate is 0 when $t = 0$. The rationality of this fitting condition should be further assessed. However, considering that equation (12) has been used to the practical applications of velocity estimation in [36], we follow the same fitting condition in this paper.

Evaluating the expression of the ATI phase, the ATI phase is determined from three motion parameters of the moving target. That is, azimuth velocity v_{x0}, range velocity v_{y0}, and acceleration a_{y0}. However, in the other references, such as [38, 42, 43], equation (13) is modified as

$$\angle\text{ATI} \simeq \frac{k\, d\, y_0 v_{y0}}{R_0 v_a}. \tag{14}$$

Comparing (13) with (14), we find that in (14), the effect of v_{x0} and a_{y0} on the ATI phase is ignored, which is because one equation cannot solve three unknown parameters simultaneously. The error due to this approximation is acceptable in many cases. As discussed in [36], when v_{x0} and a_{y0} are nonzero, the overall shift in the ATI phase increases or decreases depending on their sign. In practice, we cannot guarantee the sign of the motion parameters, so replacing (13) with (14) is a reasonable choice. The above conclusions are derived for airborne SAR only, but it is easy to be extended to spaceborne SAR. We apply (13) for further discussion in the following sections.

3. The FrFT and the Proposed Method

In this section, we briefly introduce the definition and applications of FrFT and propose a method for estimating ship motion parameters.

3.1. FrFT. The FrFT has many applications in solving differential equations, quantum mechanics, and quantum optics, pattern recognition, and studying time-frequency distribution [44]. Chirp rate estimates from the LFM signal is one of the most significant applications for FrFT.

The FrFT represents a generalized form of the classical Fourier transform, and the FrFT definition is given as follows:

$$X_\alpha(u) = \int_{-\infty}^{\infty} x(t) K_\alpha(t, u)\mathrm{d}t, \tag{15}$$

where α is the order of FrFT, corresponding to a rotation angle $\theta = \alpha(\pi/2)$, and $K_\alpha(t, u)$ is the kernel function of the FrFT. The intact definition is

$$K_\alpha(t, u) = \begin{cases} \sqrt{\dfrac{1 - j\cot\alpha}{2\pi}}\, e^{j\left(\left(\left(u^2 + t^2\right)/2\right)\cot\alpha - ut\csc\alpha\right)}, & \text{if}, \alpha \neq n\pi, \\ \delta(t - u), & \text{if}, \alpha = 2n\pi, \\ \delta(t + u), & \text{if}, \alpha = (2n + 1)\pi. \end{cases} \tag{16}$$

Applied to LFM signals, compared with the energy spread in the Fourier transform domain, the energy in the FrFT domain is more concentrated. The order α of the FrFT facilitates finding the rotation that optimizes the representation in the time-frequency domain. Herein, optimization means that the target energy is the most concentrated.

3.2. Proposed Method. In the general linear chirp formula $\exp j2\pi(kt^2 + bt + c)$, the chirp rate is k, and the optimum transform angle that best focuses on the fractional Fourier spectrum of the chirp signal is defined as [44]

$$\theta_{\text{opt}} = -\tan^{-1}\left(\frac{F_s^2/N}{2k}\right), \tag{17}$$

where F_s is the sampling frequency and N is the number of samples.

Adapting the equation for the azimuth LFM signal, (17) is replaced [44] as

$$\theta_{\text{opt}_{\text{az}}} = -\tan^{-1}\left(\frac{\text{PRF}^2/N}{2k_{\text{az}}}\right), \tag{18}$$

where PRF is the pulse repetition frequency, N is the number of samples in the azimuth, and k_{az} represents the azimuth rate.

There is a relationship between phase and chirp rate:

$$k = -\frac{1}{2\pi}\frac{\mathrm{d}^2\phi}{\mathrm{d}t^2}, \tag{19}$$

where k is chirp rate and ϕ is echo phase.

Similar to the derivation in [16], on the basis of (9) and (10), we can obtain the chirp rate of the moving target echo after range compression for the fore channels as

$$k_{\text{fore}} = k_{\text{SAR}} + \frac{2}{\lambda R_0}\left[-2v_a v_{x0} + v_{x0}^2 + v_{y0}^2\left(1 - \left(\frac{y_0^2}{R_0^2}\right)\right) + y_0 a_{y0}\right] = k_{\text{SAR}} + \Delta k_1, \tag{20}$$

where $k_{\text{SAR}} = (2v_a^2/\lambda R_0)$ is the chirp rate for the stationary scene.

After azimuth compression, the chirp rate expression for the fore channel can be obtained as follows:

$$k_{\text{fore.a}} = \frac{k_{\text{SAR}}^2}{\Delta k_1} + k_{\text{SAR}}. \tag{21}$$

Equation (21) is the theoretical chirp rate. Clearly, from (18) and (21), we can obtain the following equation:

$$-\frac{\text{PRF}^2}{N}\cot\left(\theta_{\text{opt1}}\right) = \frac{k_{\text{SAR}}^2}{(2/\lambda R_0)\left[-2v_a v_{x0} + v_{x0}^2 + v_{y0}^2\left(1 - \left(y_0^2/R_0^2\right)\right) + y_0 a_{y0}\right]} + k_{\text{SAR}}, \tag{22}$$

where θ_{opt1} is the optimum transform angle corresponding to the fore channel.

Combining (12), (13), and (22), we obtain an equation set relating v_{x0}, v_{y0}, and a_{y0}. From this equation set, we can solve the three unknown motion parameters. Generally speaking, it is difficult to obtain analytic solutions from a nonlinear equation set. Fortunately, the equation set derived in our paper can be obtained using mathematical manipulation.

We use the following variable substitution:

$$p = \left(v_{x0} - v_a\right)^2 + v_{y0}^2\left(1 - \frac{y_0^2}{R_0^2}\right) + y_0 a_{y0}. \tag{23}$$

Then, equations (12), (13), and (22) can be rewritten as follows:

$$t_{\text{img}} = -\frac{y_0 v_{y0}}{p}, \tag{24}$$

$$\angle\text{ATI} = \frac{k\,d\,y_0 v_{y0}}{2R_0}\cdot\left(\frac{1}{v_a} - \frac{\left(v_{x0} - v_a\right)}{p}\right), \tag{25}$$

$$-\frac{\text{PRF}^2}{N}\cot\left(\theta_{\text{opt1}}\right) = \left(\frac{k_{\text{SAR}}^2}{(2p/\lambda R_0) - k_{\text{SAR}}}\right) + k_{\text{SAR}}. \tag{26}$$

First, from (26), we can easily obtain the value of p according to equation (27), i.e.,

$$p = \frac{\lambda R_0}{2}\left(\left(\frac{k_{\text{SAR}}^2}{-\left(\text{PRF}^2/N\right)\cot\left(\theta_{\text{opt1}}\right) - k_{\text{SAR}}}\right) + k_{\text{SAR}}\right). \tag{27}$$

We can estimate v_{y0} from (24):

$$v_{y0} = -\frac{p}{y_0}t_{\text{img}}. \tag{28}$$

Next, we notice that v_{x0} can be resolved from (25) as (29), because the estimation of v_{y0} has been already calculated:

$$v_{x0} = \left(\frac{1}{V_a} - \frac{2R_0\angle\text{ATI}}{k\,d\,y_0 v_{y0}}\right)p + V_a. \tag{29}$$

Finally, we obtain the estimation of a_{y0} from (23) and (26) as

$$a_{y0} = \frac{p - \left(v_{x0} - v_a\right)^2 + v_{y0}^2\left(1 - \left(y_0^2/R_0^2\right)\right)}{y_0}. \tag{30}$$

The overall motion parameter estimation procedure is summarized in Figure 2, which involves four steps detailed as follows:

Step 1. Generate the ATI image of the moving target: conjugate multiply the fore channel image with aft channel image to obtain the ATI image.

Step 2. Obtain peak time and ATI phase: determine the peak time from the fore channel image on the basis of pixel magnitude. Then, retrieve the ATI phase from the maximum response in the ATI image.

Step 3. Calculate the chirp rate: utilize global FrFT map to obtain the optimum rotation angle from the fore channel image (the strategy in [16] can be exploited to obtain the global FrFT map, see [16] for details). Then, calculate the corresponding chirp rate of the moving target echo.

Step 4. Estimate the motion parameters: exploit formulae (28)–(30) to estimate the azimuth velocity, range velocity, and acceleration for the moving target.

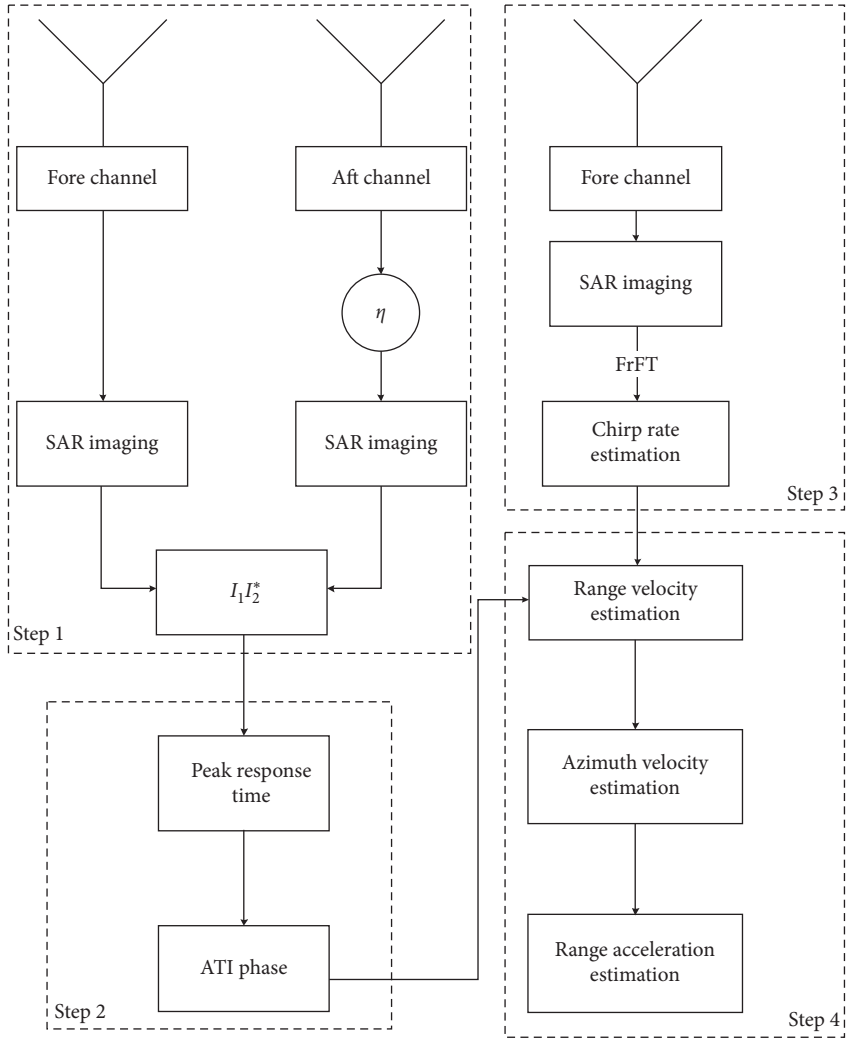

Figure 2: Flowchart describing the proposed method where the notation η denotes the image registration operator.

4. Simulation Results

In this section, we compare our proposed method with the method presented in [16] and illustrate our method's superiority. The method in [16] is implemented in image domain and the methods based on multichannel SAR are often achieved in RD domain [17]. In the general case, the SAR systems such as TanDEM-X could provide high-resolution complex image data [45], so the method implemented in image domain might have more practicability than the method achieved in RD domain. Therefore, in the scope of this study, we consider the velocity estimation realized in image domain rather than RD domain.

4.1. Method Description in [16]. The moving target echo model in the contrast method is very similar to that proposed in this study. For the single-channel SAR, the model must be simplified. Compared with (20), the influences of v_{y0} and a_{y0} on the chirp rate are ignored in [16]. Hence, the chirp rate of the moving target echo after the range compression for the fore channels is

$$\begin{aligned} k'_{\text{fore}} &= k_{\text{SAR}} + \frac{2}{\lambda R_0}\left[-2v_a v_{x0} + v_{x0}^2\right] \\ &= k_{\text{SAR}} + \Delta k'_1. \end{aligned} \tag{31}$$

Therefore, the chirp rate after azimuth compression can be expressed as

$$k'_{\text{fore}.a} = \frac{k_{\text{SAR}}^2}{\Delta k'_1} + k_{\text{SAR}}. \tag{32}$$

According to the above derivation, azimuth velocity can be estimated from (33) as

$$v_{\text{az}} = v_a\left(1 - \sqrt{1 + \left(\frac{2v_a^2}{\lambda R_0\left(\text{PRF}^2/N\right)\cot\beta_{\text{opt}} - 2v_a}\right)}\right), \tag{33}$$

where β_{opt} is the optimum transform angle corresponding to the single channel.

4.2. Simulation Experiments. We have described the principle of the method in [16], which generalized the FrFT from the signal domain to the image domain. As a result, we can compare the two methods in the image domain. Table 1 provides the simulation parameters for the ATI imaging; the simulation parameters are identical to the DC-8 platform in the [46]. The data collected from the system have been widely applied to ship detection [47, 48]. Figures 3(a) and 3(b) correspond to the simulated images of the fore and aft channels, respectively. X-axis of images represents the range, and y-axis represents azimuth.

$$P = \frac{|E - T|}{T} * 100\%, \tag{34}$$

From Figure 3, we can obtain the complex image data after conjugate multiplying. Then, the peak response time t_{img} and ATI phase can be resolved from the ATI image. For the fore channel image, we extract the azimuth line containing the pixel with the greatest magnitude to calculate the azimuth chirp rate based on the FrFT.

Assuming the target moves along the azimuth line, our method can be reduced to the contrast method because the values of range velocity and acceleration are zero. Table 2 provides the estimation and Figure 4 presents the absolute error of the estimation, x-axis denotes the true azimuth velocity, and y-axis denotes the absolute errors between the true and estimated azimuth velocity. In Table 2, the percent error is calculated as follows:where P is the percent error, E is the estimation of azimuth velocity, and T is the true value of azimuth velocity.

From Table 2 and Figure 4, the contrast method has a comparable estimation accuracy in the absence of range velocity and acceleration. However, in practice, the ship usually moves with an angle from the azimuth line. Thus, the range velocity and acceleration are nonzero, and the approximation in [16] may result in an additional error. Next, we consider the estimation results from our method and the contrast method in the presence of range velocity and acceleration. Table 3 provides the estimation results from our method and the contrast method; the range velocity and acceleration are focused on 4 m/s and 0.1 m/s^2, respectively, and the azimuth velocity varies from 1 m/s to 15 m/s. Analogously, in Table 4, the azimuth velocity and range acceleration are focused on 4 m/s and 0.1 m/s^2, respectively, and the range velocity varies from 1 m/s to 10 m/s. The azimuth and range velocity in Table 5 are simultaneously focused on 4 m/s, and the range acceleration varies from 0.01 m/s^2 to 0.1 m/s^2. The estimated results of different simulated scenario are shown in Figures 5 and 6. Figure 5(a) represents the absolute errors between the true and estimated azimuth velocity, Figure 5(b) represents the contrast trial between the methods in [16] and our proposed method, Figure 5(c) represents the absolute errors between the true and estimated range velocity, and Figure 5(d) represents the absolute errors between the true and estimated range acceleration.

Table 1: Simulation parameters for ATI imaging.

Height	8693.4 m
Velocity	214.77 m/s
Transmit bandwidth	40 MHz
Slant range resolution	3.8 m
Imaging algorithm	R-D
Range window	Hamming
Baseline	2.0794 m
Wavelength	0.057 m
Sampling rate	90 MHz
Azimuth resolution	3.3 m
Angle of incidence	$\pi/4$
Band	C

As shown in Table 3 and Figure 5, our proposed method provides a more accurate estimation than the contrast method for azimuth velocity. The value estimated using the contrast method is biased from the truth above 2 m/s; as the azimuth velocity increases, the bias becomes larger. A similar observation can be made for the proposed method, but the bias is only 0.21 m/s when the azimuth velocity is 15 m/s. The difference is due to the moving target echo model. In comparison, the contrast method derived the azimuth velocity estimation expression by neglecting the range velocity and acceleration.

Comparing Table 2 with Table 3, the performance of the contrast method significantly degrades with range velocity and acceleration. In addition to the azimuth velocity, the proposed method can guarantee estimation accuracy for range velocity and acceleration.

From Table 4 and Figure 6, the influence of range velocity on azimuth velocity estimation can be analysed more clearly. When the range velocity is 1 m/s, the absolute error in the azimuth velocity estimation is about 0.4 m/s; as the range velocity increases to 10 m/s, the absolute error increases to 0.8 m/s. This observation further verifies the effect resulting from the range velocity.

Table 5 and Figure 7 indicate the influence of range acceleration on the azimuth velocity estimation. When the range acceleration is 0.01 m/s^2, the absolute error is about 0.1 m/s, and as the range acceleration increases to 0.1 m/s^2, the absolute error increases to 0.6 m/s. In contrast to range velocity, the range acceleration has a smaller impact on the azimuth velocity estimation. The chirp rate is likely dominated by the range velocity, except for the range acceleration has parameters shown in Table 1. Ignoring the constant, the chirp rate is dependent on the three motion parameters, as shown in Section 3:

$$k_0 = \frac{2}{\lambda R_0}\left[-2v_a v_{x0} + v_{x0}^2 + v_{y0}^2\left(1 - \frac{y_0^2}{R_0^2}\right) + y_0 a_{y0}\right]. \tag{35}$$

Equation (35) indicates that the influence of azimuth velocity on chirp rate is multiplied by the platform velocity. Therefore, it may be appropriate in [16] to neglect the influence of range velocity and acceleration for the data being collected from Radarsat-2, whose SAR sensor velocity is 7545 m/s. However, for the airborne platform, the influence

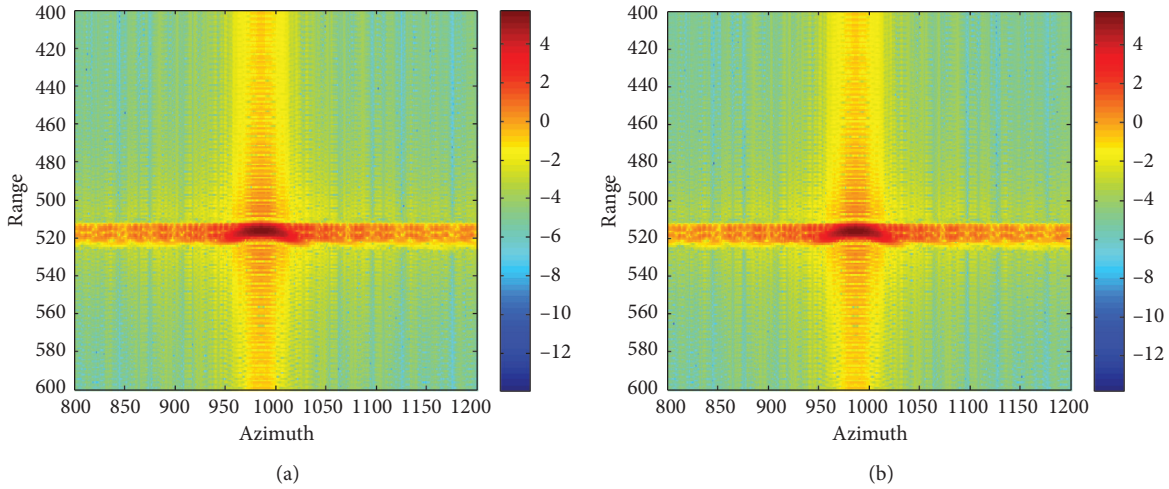

Figure 3: ATI imaging simulations: (a) simulated image of the fore channel and (b) simulated image of the aft channel.

Table 2: Azimuth velocity estimation and percent error from the contrast method for true from 1 m/s to 14 m/s.

Azimuth velocity (m/s)	Estimation based on [16] (m/s)	Percent error (%)
1	1.0078	0.8
2	2.0547	2.8
3	3.0030	0.1
4	4.0512	1.3
5	5.0730	1.5
6	6.0788	1.3
7	7.0651	1.0
8	8.0565	0.7
9	9.0607	0.7
10	10.0555	0.6
11	11.0456	0.4
12	12.0342	0.3
13	13.0547	0.4
14	14.0672	0.5

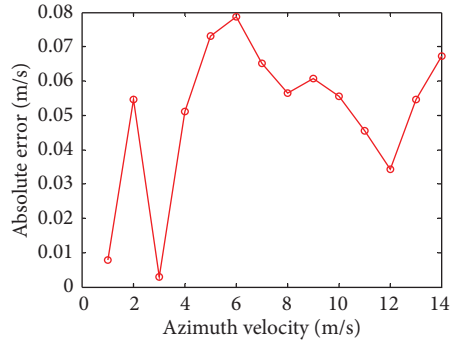

Figure 4: Absolute error in the azimuth velocity estimation from the contrast method.

of range velocity and acceleration cannot be ignored in some conditions, especially when the value of acceleration is large, such as 0.1 m/s^2 in Table 3.

All the tables show evident trends in the estimations calculated using the contrast method. It is clear that the chirp rate is a monotonic function of azimuth velocity (for small values), range velocity, and acceleration. In Tables 4 and 5, as the range velocity and acceleration, respectively, increase, the absolute errors in the azimuth velocity estimation also increase due to a lower estimation in the chirp rate.

Table 3: Estimation results as a function of azimuth velocity varying from 1 m/s to 14 m/s at $v_{y0} = 4$ m/s and $a_{y0} = 0.1$ m/s^2.

Azimuth velocity (m/s)	Estimation in this paper (m/s)	Percent error (%)	Estimation based on [16] (m/s)	Percent error (%)	Range velocity estimation (m/s) $v_{y0} = 4$ m/s	Percent error (%)	Range acceleration estimation (m/s^2) $a_{y0} = 0.1$ m/s^2	Percent error (%)
1	1.2249	22.5	−1.2683	228.6	4.0171	0.4	0.1219	21.9
2	2.3342	16.7	−0.3318	116.6	3.9474	1.3	0.1365	36.5
3	3.3023	10.1	0.6210	79.3	4.1068	2.7	0.1328	32.8
4	4.1179	3.0	1.5718	60.7	4.0101	0.3	0.1130	13.0
5	5.1585	3.2	2.5207	50.0	4.0141	0.4	0.1151	15.1
6	6.1167	2.0	3.4673	42.2	4.0108	0.3	0.1118	11.8
7	7.0700	1.0	4.4118	37.0	4.0067	0.2	0.1083	8.3
8	8.1583	2.0	5.3538	33.1	4.0159	0.4	0.1133	13.3
9	9.1473	1.7	6.2932	30.1	4.0154	0.4	0.1120	12.0
10	10.1431	1.4	7.2298	27.7	4.0156	0.4	0.1112	11.2
11	11.1591	1.5	8.1636	25.8	4.0182	0.5	0.1116	11.6
12	12.1664	1.4	9.0942	24.2	4.0199	0.5	0.1114	11.4
13	13.1723	1.3	10.0214	22.9	4.0216	0.5	0.1112	11.2
14	14.1762	1.3	10.9451	21.8	4.0231	0.6	0.1108	10.8
15	15.2149	1.4	11.8649	20.9	4.0296	0.7	0.1124	12.4

Table 4: Estimation results as a function of range velocity varying from 1 m/s to 10 m/s at $v_{x0} = 4$ m/s and $a_{y0} = 0.1$ m/s^2.

Azimuth velocity estimation in this paper (m/s) $v_{x0} = 4$ m/s	Percent error (%)	Azimuth velocity estimation based on [16] (m/s) $v_{x0} = 4$ m/s	Percent error (%)	Range velocity estimation (m/s) $v_{y0} = 4$ m/s	Percent error (%)	Range acceleration (m/s^2)	Range acceleration estimation (m/s^2)	Percent error (%)
3.8795	3.0	3.6064	9.8	3.9888	0.3	0.01	0.0073	27.0
3.9533	1.2	3.3760	15.6	3.9957	0.1	0.02	0.0221	10.5
3.9400	1.5	3.1467	21.3	3.9945	0.1	0.03	0.0313	4.3
4.0001	0.0	2.9185	27.0	4.0000	0.0	0.04	0.0452	13.0
4.0044	0.1	2.6914	32.7	4.0004	0.0	0.05	0.0555	11.0
4.0620	0.2	2.4653	38.4	4.0055	0.1	0.06	0.0693	15.5
4.0076	0.2	2.2404	44.0	4.0007	0.0	0.07	0.0757	8.1
4.0617	0.2	2.0165	49.6	4.0054	0.1	0.08	0.0893	11.6
4.0138	0.3	1.7937	55.2	4.0012	0.0	0.09	0.0961	6.8
4.1179	0.3	1.5718	60.7	4.0101	0.3	0.10	0.1130	13.0

Table 5: Estimation results as a function of range acceleration varying from 0.01 m/s^2 to 0.1 m/s^2 at $v_{x0} = 4$ m/s and $v_{y0} = 4$ m/s.

Azimuth velocity estimation in this paper (m/s) $v_{x0} = 4$ m/s	Percent error (%)	Azimuth velocity estimation based on [15] (m/s) $v_{x0} = 4$ m/s	Percent error (%)	Range velocity (m/s)	Range velocity estimation (m/s)	Percent error (%)	Range acceleration estimation (m/s^2) $a_{y0} = 0.1$ m/s^2	Percent error (%)
3.9711	0.7	1.7165	57.1	1	0.9994	0.1	0.0968	3.2
4.0935	2.3	1.6876	57.8	2	2.0040	0.2	0.1061	6.1
4.1339	3.4	1.6393	59.0	3	3.0086	0.3	0.1110	11.0
4.1179	3.0	1.5718	60.8	4	4.0101	0.3	0.1130	13.0
4.2857	7.1	1.4852	62.9	5	5.0303	0.6	0.1279	27.9
4.2421	6.1	1.3796	65.5	6	6.0307	0.5	0.1298	29.8
4.2519	6.3	1.2550	68.6	7	7.0381	0.5	0.1328	32.8
4.2815	7.0	1.1116	72.2	8	8.0471	0.6	0.1446	44.6
4.2567	6.4	0.9497	76.3	9	9.0480	0.5	0.1504	50.4
4.2485	6.2	0.7693	80.8	10	10.0513	0.5	0.1581	58.1

However, from Table 3, the absolute errors in the azimuth velocity are almost 0.6 m/s. Small fluctuations are probably caused by different FrFT estimation precisions. In contrast to the trends in the results from percentage of the azimuth velocity, the proposed method is not evident. This is because the proposed method requires measuring more quantities

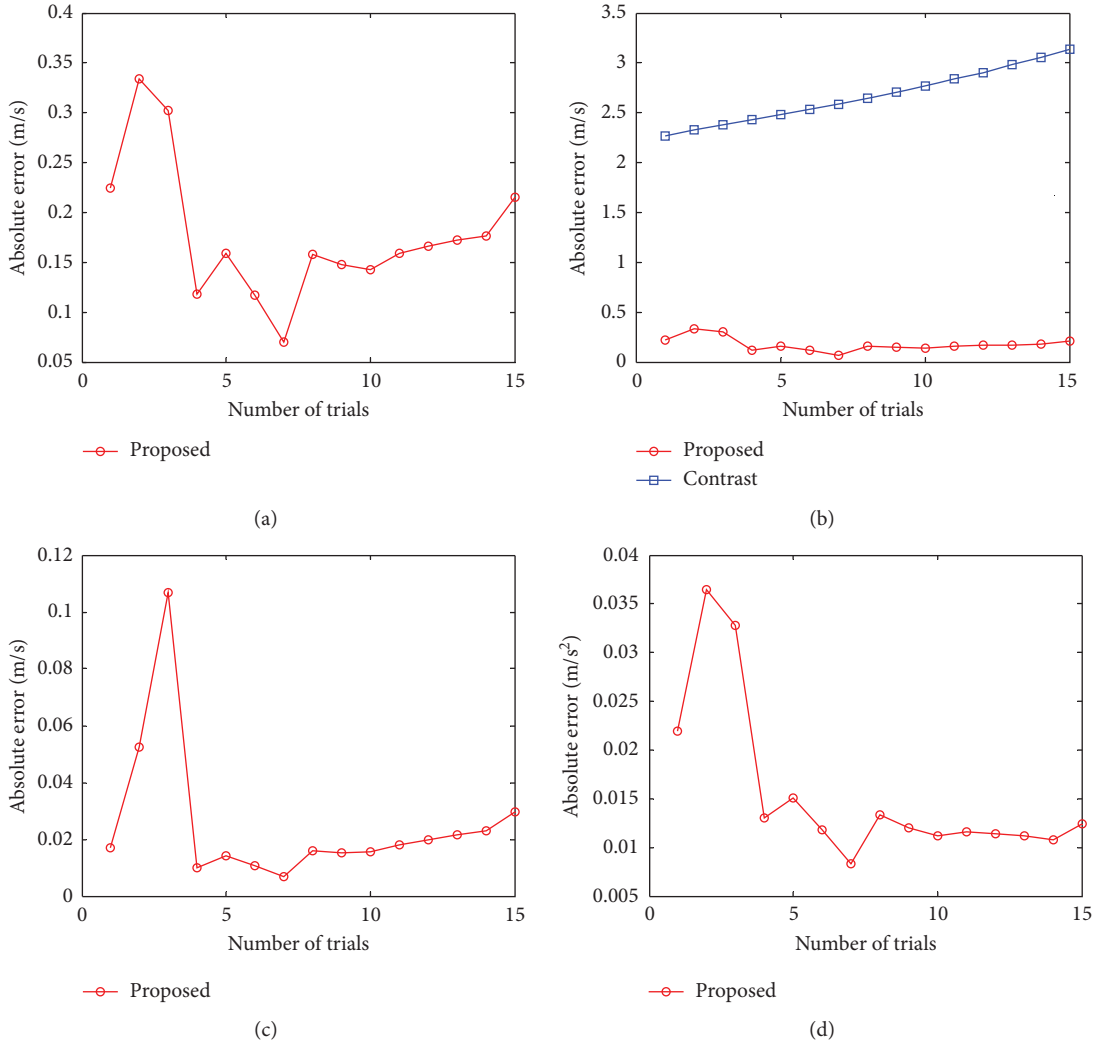

FIGURE 5: Estimation results as a function of azimuth velocity varying from 1 m/s to 14 m/s at $v_{y0} = 4$ m/s and $a_{y0} = 0.1$ m/s^2. (a) Absolute error in the azimuth velocity estimation using the proposed method, (b) a comparison of the errors from the proposed method and contrast method, (c) absolute error in the range velocity estimation using the proposed method, and (d) absolute error in the range acceleration estimation using the proposed.

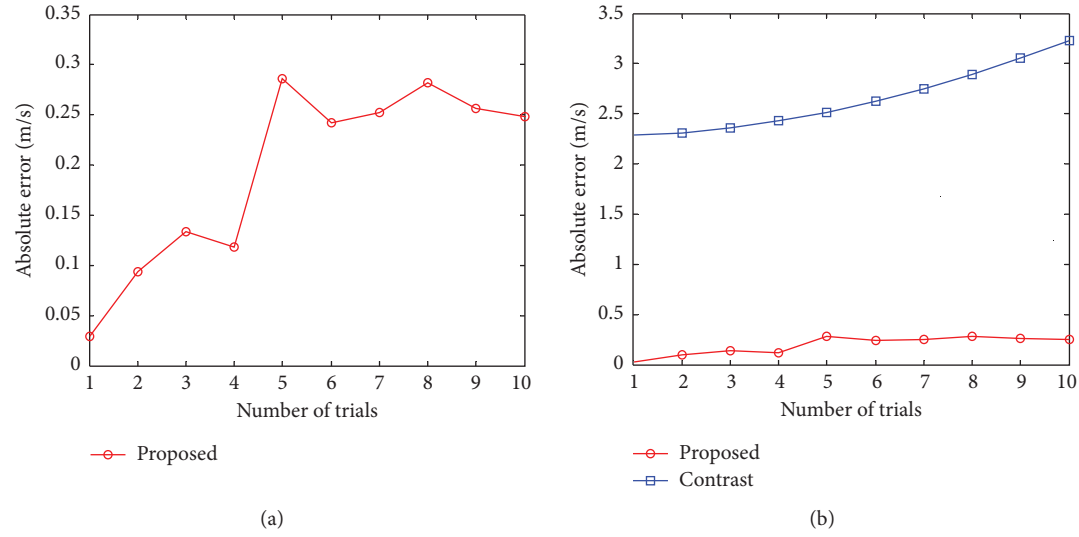

FIGURE 6: Continued.

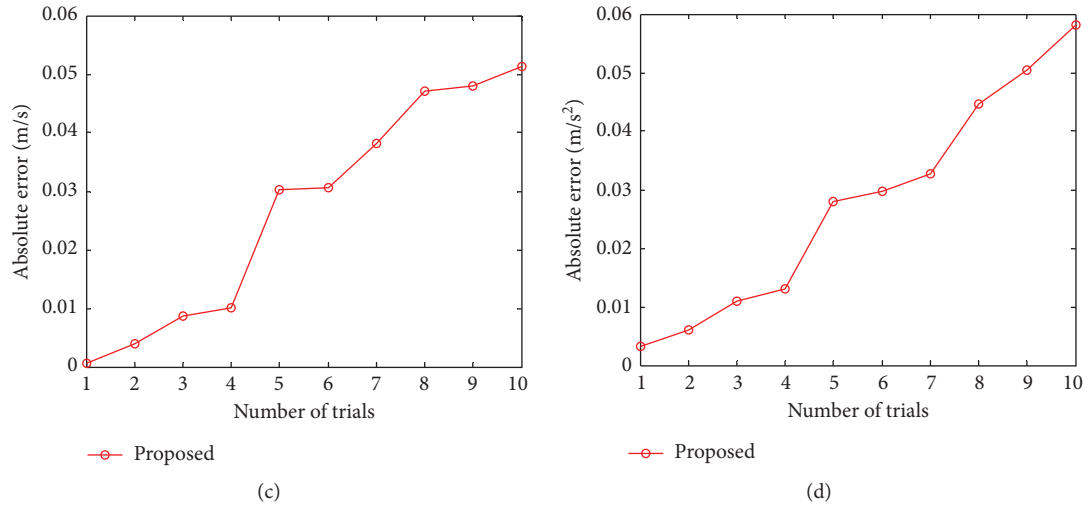

FIGURE 6: Estimation results as a function of range velocity varying from 1 m/s to 10 m/s at $v_{x0} = 4$ m/s, $a_{y0} = 0.1$ m/s^2. (a) Absolute error in the azimuth velocity estimation using the proposed method, (b) a comparison of the errors from the proposed method and contrast method, (c) absolute error in the range velocity estimation using the proposed method, and (d) absolute error in the range acceleration estimation using the proposed method.

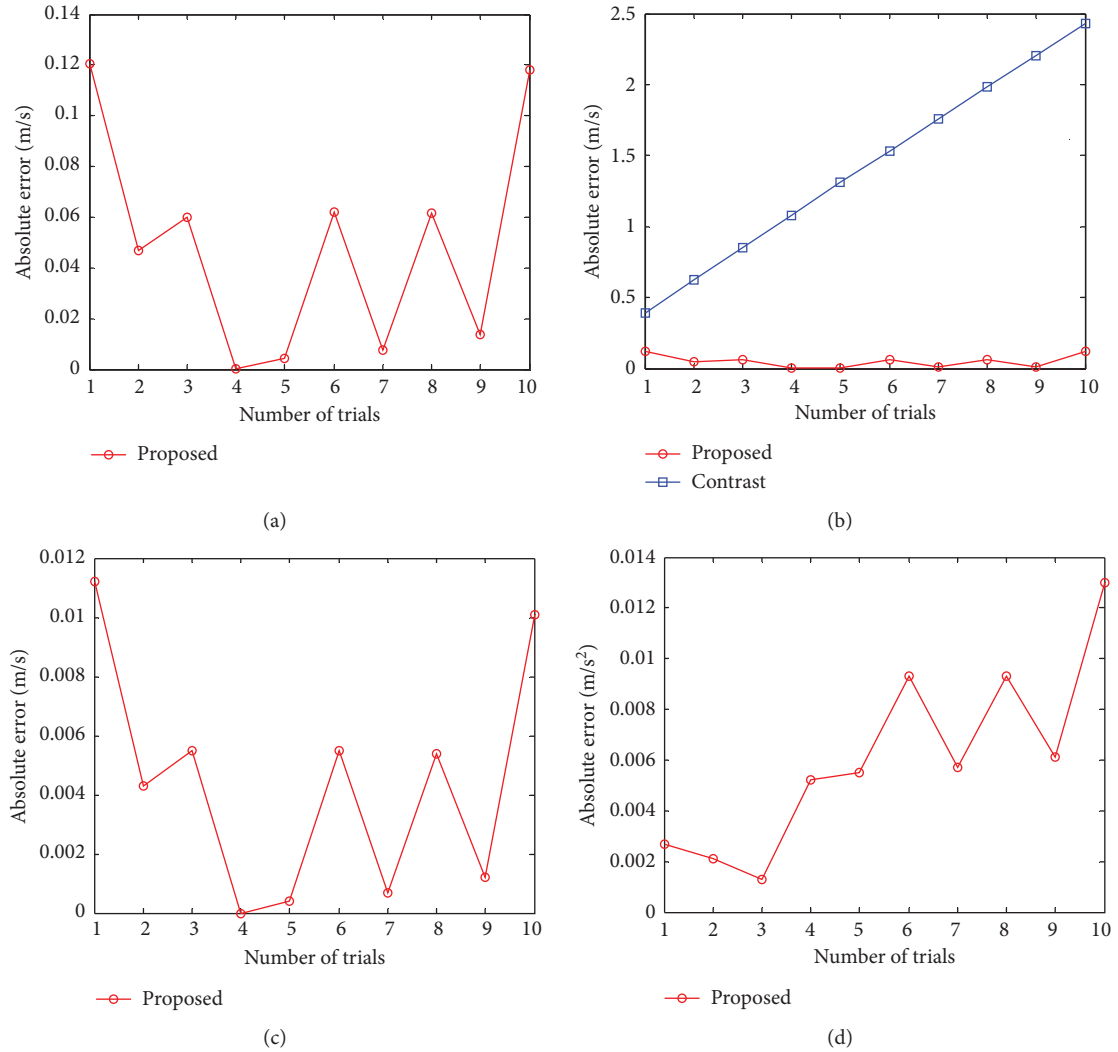

FIGURE 7: Estimation results as a function of range acceleration varying from 0.01 m/s^2 to 0.1 m/s^2 at $v_{x0} = 4$ m/s and $v_{y0} = 4$ m/s. (a) Absolute error in the azimuth velocity estimation using the proposed method, (b) a comparison of the errors from the proposed method and contrast method, (c) absolute error in the range velocity estimation using the proposed method, and (d) absolute error in the range acceleration estimation using the proposed method.

from the images, which leads to inevitable measurement errors, so the estimation fluctuates more and does not have evident trends.

5. Conclusion

In this study, we introduced a novel velocity estimation algorithm for moving ships based on the FrFT and ATI. Compared with the method in [16], the proposed method fully exploits the information advantages of multichannel SAR, combining the FrFT and ATI to construct equation sets that can achieve multiple motion parameter estimations. From the experiments in Section 4, the proposed method obtained a more accurate estimation for azimuth velocity compared to the contrast method, and the estimated range velocity and acceleration are relatively accurate.

Moreover, the chirp rates measured at different parts of a moving ship are not constant because they are modulated by the ship's three-axis motion.

The proposed solution to this problem is similar to the contrast method. In [16], the authors applied the FrFT locally to segments extracted around maximum values from the input signal. The estimation accuracy is determined based on the constructed model. In this study, the model is the same as the commonly used model in [36] and a good performance is obtained. However, for a moving ship (or even a "stationary" ship), the heave motion must be included or modelled to be of practical use. In addition, even without including the heave motion components in the ship range history model, the acceleration component in the along-track direction introduces nonlinearity in the signal chirp. We have no reason to doubt that a more accurate estimation could be theoretically acquired using the model in [36]; however, this is challenging at present and should be the subject of future research. Therefore, in this study, we only consider azimuth velocity, range velocity, and acceleration. In this case, the received echo can be approximated well using the LFM signal. Moreover, our proposed method is not suitable for spaceborne SAR because of earth surface curvature and topography. There is a large deviation if the flat earth approximation is applied to the spaceborne SAR data [49].The multichannel SAR, which contains three or more channels, and nonlinearity and nonlinearity in the signal chirp, caused by azimuth acceleration, will be considered in future research to achieve accurate motion parameter estimations.

Data Availability

The SAR simulation data used to support the findings of this study are currently under embargo.

Conflicts of Interest

The authors declare that there are no conflicts of interest regarding the publication of this paper.

Authors' Contributions

Conceptualization and funding acquisition were carried out by K.H. and C.C.; methodology was developed by C.C. and Y.L.; validation was done by Y.L., C.C., and L.Z.; formal analysis was conducted by Y.L. and K.O.; investigation was carried out by K.O., K.H., and C.C.; writing (original draft preparation) was performed by Y.L. and K.H.; writing (review and editing) was performed by C.C., K.H., and L.Z; supervision was provided by K.H; project administration was carried out by C.C.

Acknowledgments

This research was funded by the National Science Foundation of China under grant no. 71471174. This work was supported in part by the National Natural Science Foundation of China under Project 41822105, in part by Key Research Plan of Hunan Province under Project 2019SK2173, in part by the Field Foundation under Project 61404160109, and in part by the Fundamental Research Funds for the Central Universities under Project 2682020ZT34.

References

[1] Cumming and F. Wong, *Digital Processing of Synthetic Aperture Radar Data: Algorithms and Implementation*, Artech House Publishers, Norwood, MA, USA, 2005.

[2] C. E. Livingstone, I. Sikaneta, C. H. Gierull et al., "An airborne synthetic aperture radar (SAR) experiment to support RADARSAT-2 ground moving target indication (GMTI)," *Canadian Journal of Remote Sensing*, vol. 28, no. 6, pp. 794–813, 2002.

[3] R. Raney, "Synthetic aperture imaging radar and moving targets," *IEEE Transactions on Aerospace and Electronic Systems*, vol. AES-7, no. 3, pp. 499–505, 1971.

[4] W. Alpers and C. Bruening, "On the relative importance of motion-related contributions to the SAR imaging mechanism of ocean surface waves," *IEEE Transactions on Geoscience and Remote Sensing*, vol. GE-24, no. 6, pp. 873–885, 1986.

[5] M. D. Graziano, M. D'Errico, and G. Rufino, "Ship heading and velocity analysis by wake detection in SAR images," *Acta Astronautica*, vol. 128, pp. 72–82, 2016.

[6] J. K. E. Tunaley, "The estimation of ship velocity from SAR imagery," in *Proceedings of the IEEE International Geoscience and Remote Sensing Symposium IGARSS '03*, pp. 191–193, Toulouse, France, July 2003.

[7] G. Zilman, A. Zapolski, and M. Marom, "The speed and beam of a ship from its wake's SAR images," *IEEE Transactions on Geoscience and Remote Sensing*, vol. 42, no. 10, pp. 2335–2343, 2004.

[8] A. C. Copeland, G. Ravichandran, and M. M. Trivedi, "Localized radon transform-based detection of ship wakes in SAR images," *IEEE Transactions on Geoscience and Remote Sensing*, vol. 33, no. 1, pp. 35–45, 1995.

[9] P. Courmontagne, "An improvement of ship wake detection based on the radon transform," *Signal Processing*, vol. 85, no. 8, pp. 1634–1654, 2005.

[10] D. Carona and P. Marques, "Vessel detection and velocity estimation using SAR amplitude images," Portuguese Foundation for Science and Technology, Lisbon, Portugal, Project PTDC/EEA-TEL/71996, 2006.

[11] P. W. Vachon, C. Kabatoff, and R. Quinn, "Operational ship detection in Canada using RADARSAT," in *Proceedings of the IEEE IGARSS*, pp. 998–1001, Quebec, Canada, July 2014.

[12] A. Renga and A. Moccia, "Use of doppler parameters for ship velocity computation in SAR images," *IEEE Transactions on Geoscience and Remote Sensing*, vol. 54, no. 7, pp. 3995–4011, 2016.

[13] A. Radius and P. Marques, "Velocity estimation of moving ships using c-band SLC SAR data," in *Proceedings of the 2015 Sensor Signal Processing for Defence (SSPD)*, Edinburgh, UK, September 2015.

[14] M. V. Dragosevic and P. W. Vachon, "Estimation of ship radial speed by adaptive processing of RADARSAT-1 fine mode data," *IEEE Geoscience and Remote Sensing Letters*, vol. 5, no. 4, pp. 678–682, 2008.

[15] M. Kirscht, "Detection and imaging of arbitrarily moving targets with single-channel SAR," *IEE Proceedings—Radar Sonar and Navigation*, vol. 150, no. 1, pp. 7–11, 2003.

[16] R. Pelich, N. Longepe, G. Mercier, and G. Hajduch, "Vessel refocusing and velocity estimation on SAR imagery using the fractional fourier transform," *IEEE Transactions on Geoscience and Remote Sensing*, vol. 54, no. 3, pp. 1670–1684, 2016.

[17] P. Huang, G. Liao, Z. Yang, and J. Ma, "An approach for refocusing of ground fast-moving target and high-order motion parameter estimation using radon-high-order time-chirp rate transform," *Digital Signal Processing*, vol. 48, pp. 333–348, 2016.

[18] M. Soccorsi and S. Lehner, "Single channel complex SAR images ship speed and current motion retrieval," in *Proceedings of the 2010 IEEE Gold Remote Sensing Conference*, pp. 1–3, Livorno, Italy, April 2010.

[19] D. Ao, M. Datcu, G. Schwarz, and C. Hu, "Moving ship velocity estimation using TanDEM-X data based on sub-aperture decomposition," *IEEE Geoscience and Remote Sensing Letters*, vol. 15, no. 10, pp. 1560–1564, 2018.

[20] B. Filippo, "COSMO-SkyMed staring spotlight SAR data for micro-motion and inclination angle estimation of ships by pixel tracking and convex optimization," *Remote Sensing*, vol. 11, no. 7, p. 766, 2019.

[21] M. Back, D. Kim, S.-W. Kim, and J.-S. Won, "Two-dimensional ship velocity estimation based on KOMPSAT-5 synthetic aperture radar data," *Remote Sensing*, vol. 11, no. 12, p. 1474, 2019.

[22] E. Makhoul, S. V. Baumgartner, M. Jager, and A. Broquetas, "Multichannel SAR-GMTI in maritime scenarios with F-SAR and TerraSAR-X sensor," *IEEE Journal of Selected Topics in Applied Earth Observations and Remote Sensing*, vol. 8, no. 11, pp. 5052–5067, 2015.

[23] I. Sikaneta and C. Gierull, "Ground moving target detection for along-track interferometric SAR data," in *Proceedings of the 2004 IEEE Aerospace Conference*, pp. 2227–2235, Big Sky, MT, USA, March 2004.

[24] J. Ward, "Space-time adaptive processing for airborne radar," in *Proceedings of the IEE Colloquium on Space-Time Adaptive Processing*, pp. 2/1–2/6, London, UK, April 1995.

[25] M. Dragosevic, M. Henschel, and C. Livingstone, "An adaptive technique for estimating ship motion in SAR data," in *Proceedings of the European Radar Conference EURAD*, Munich, Germany, October 2007.

[26] Y. Jiang, J. L. Chen, Y. Wang, and W. F. Wang, "The GMTI technology of spaceborne SAR," *Aerospace Shanghai*, vol. 6, pp. 60–64, 2009.

[27] S. Chiu, "Application of fractional fourier transform to moving target indication via along-track interferometry," *EURASIP Journal on Advances in Signal Processing*, vol. 2005, no. 20, pp. 3293–3303, Article ID 980786, 2005.

[28] D. Cerutti-Maori and I. Sikaneta, "A generalization of DPCA processing for multichannel SAR/GMTI radars," *IEEE Transactions on Geoscience and Remote Sensing*, vol. 51, no. 1, pp. 560–572, 2013.

[29] G. Gao and G. Shi, "Ship detection in dual-channel ATI-SAR based on the notch filter," *IEEE Transactions on Geoscience and Remote Sensing*, vol. 55, no. 8, pp. 4795–4810, 2017.

[30] R. M. Goldstein and H. A. Zebker, "Interferometric radar measurement of ocean surface currents," *Nature*, vol. 328, no. 6132, pp. 707–709, 1987.

[31] C. W. Chen, "Performance assessment of along-track interferometry for detecting ground moving targets," in *Proceedings of the IEEE National Radar Conference*, pp. 99–104, Philadelphia, PA, USA, April 2004.

[32] R. Romeiser, H. Runge, S. Suchandt et al., "Current measurements in rivers by spaceborne along-track InSAR," *IEEE Transactions on Geoscience and Remote Sensing*, vol. 45, no. 12, pp. 4019–4031, 2007.

[33] R. Romeiser, H. Breit, M. Eineder, and H. Runge, "Demonstration of current measurements from space by along-track SAR interferometry with SRTM data," in *Proceedings of the IEEE International Geoscience and Remote Sensing Symposium IGARSS*, pp. 158–160, Toronto, Canada, June 2002.

[34] R. Romeiser, S. Suchandt, H. Runge, U. Steinbrecher, and S. Grunier, "First analysis of TerraSAR-X along-track InSAR-derived current fields," *IEEE Transactions on Geoscience and Remote Sensing*, vol. 48, no. 2, pp. 820–829, 2009.

[35] S. V. Baumgartner and G. Krieger, "Acceleration-independent along-track velocity estimation of moving targets," *IET Radar, Sonar and Navigation Letters*, vol. 4, no. 3, pp. 474–487, 2010.

[36] J. J. Sharma, C. H. Gierull, and M. J. Collins, "The influence of target acceleration on velocity estimation in dual-channel SAR-GMTI," *IEEE Transactions on Geoscience and Remote Sensing*, vol. 44, no. 1, pp. 134–147, 2006.

[37] S. Gradshteyn, I. M. Ryzhik, and R. H. Romer, "Tables of integrals, series, and products," *American Journal of Physics*, vol. 56, no. 10, pp. 958–958, 1988.

[38] J. Sharma, "The influence of target acceleration on dual-channel SAR-GMTI (synthetic aperture radar ground moving target indication) data," M. S. thesis, Univ. Calgary, Calgary, Canada, 2004.

[39] M. V. Dragosevic, M. D. Henschel, and C. E. Livingstone, "An approach to ship motion estimation with dual-receive antenna SAR," in *Proceedings of the 2008 IEEE Radar Conference*, vol. 20, no. 12, pp. 1–6, Rome, Italy, May 2008.

[40] D. Henschel and C. E. Livingstone, "Observation of vessel heave with airborne SAR," in *Proceedings of the Ocean SAR 2006 Workshop on Coastal and Marine Applications of SAR*, pp. 1–7, St. John's, Canada, October 2006.

[41] D. Henschel, M. V. Dragosevic, and C. E. Livingstone, "Characterization of vessel heave and horizontal velocities with airborne SAR," in *Proceedings of the IEEE RADAR 2007*, pp. 749–799, Boston, MA, USA, April 2007.

[42] Livingstone and I. Sikaneta, "Focusing moving targets/terrain imaged with moving-target matched filters: a tutorial," Tech. Rep. TM-2004-160, Defence Research and Development, Ottawa, Canada, 2004.

[43] H. Breit, M. Eineder, J. Holzner, H. Runge, and R. Bamler, "Synthetic aperture imaging radar and moving targets," in

Proceedings of the IGARSS, vol. 2, pp. 1187–1189, Toulouse, France, July 2003.

[44] H. M. Ozaktas, O. Arikan, M. A. Kutay, and G. Bozdagt, "Digital computation of the fractional fourier transform," *IEEE Transactions on Signal Processing*, vol. 44, no. 9, pp. 2141–2150, 1996.

[45] J.-L. Bueso-Bello, M. Martone, P. Prats-Iraola et al., "Performance analysis of TanDEM-X quad-polarization products in pursuit monostatic mode," *IEEE Journal of Selected Topics in Applied Earth Observations and Remote Sensing*, vol. 10, no. 5, pp. 1853–1869, 2017.

[46] Y. Zhang, "Along track interferometry synthetic aperture radar (ATI-SAR) techniques for ground moving target detection," Final Technical Report, Hillside Terrace Marcy, New York, NY, USA, 2006.

[47] X. Xing, K. Ji, H. Zou, J. Sun, and S. Zhou, "High resolution SAR imagery ship detection based on EXS-C-CFAR in Alpha-stable clutters," *Journal of the American Water Resources Association*, vol. 17, no. 17, pp. 316–319, 2011.

[48] C. W. Liao, Y. Wang, and X. Song, "Ship detection from polarimetric sar images," in *Proceedings of the IEEE International Geoscience and Remote Sensing Symposium IGARSS*, vol. 6, pp. 987–990, Cape Town, South Africa, July 2009.

[49] R. K. Raney, "Doppler properties of radars in circular orbits," *International Journal of Remote Sensing*, vol. 7, no. 9, pp. 1153–1162, 1986.